

# scientific data



**OPEN**  
DATA DESCRIPTOR

## GeoMIP-Pattern – a pattern scaling dataset for efficient generation of custom geoengineering scenarios

Rodrigo Muñoz-Sánchez<sup>1</sup>✉, Bernardo A. Bastien-Olvera<sup>1</sup>, Oscar Calderón<sup>1</sup>, Francisco Estrada Porrúa<sup>1,2</sup> & Miguel Altamirano<sup>2</sup>

In this paper we present GeoMIP-pattern, the first global geoengineering pattern scaling dataset. This dataset is useful to generate custom solar radiation modification scenarios and to emulate the GeoMIP model output with low data volume. Temperature, precipitation, and relative humidity patterns are derived from ScenarioMIP SSP5-8.5 and GeoMIP G6sulfur model output data using a two-step approach: the first scaling patterns are obtained by estimating a linear regression between the field of interest and the SSP5-8.5 annual global mean surface temperature, allowing for the calculation of no stratospheric aerosol injection scenarios for a global spatial grid. The second patterns are produced by regressing the field of interest on the annual global temperature difference between the G6sulfur and SSP5-8.5 experiments, which in combination with the first pattern emulates the stratospheric aerosol injection scenario. The dataset contains validation statistics, including unit root hypothesis tests novel to the field of pattern scaling, which demonstrate that the pattern slope adequately captures local changes, with most regions showing no remaining trend or nonstationarities in the residuals.

### Background & Summary

Geoengineering englobes a portfolio of anthropogenic climate modifications strategies aimed towards the reduction of the surface temperature increase associated with climate change and the emission of greenhouse gasses (GHG)<sup>1</sup>. In particular, solar radiation modification (SRM) aims to limit this temperature increase by controlling solar forcing<sup>2</sup>. Stratospheric aerosol injection (SAI) consists in the injection of SO<sub>2</sub> into the stratosphere to emulate the negative radiative forcing caused by large volcanic eruptions, such as the Pinatubo<sup>3</sup>. As happens with volcanic eruptions, such forcing is short-lived, lasting less than two years<sup>4</sup>, and thus a sustained injection of aerosols is required<sup>5,6</sup>.

The Climate Model Intercomparison Project (CMIP) is an international effort led by the Intergovernmental Panel on Climate Change (IPCC) and has the objective of estimating the uncertainty in General Circulation Models' (GCM) projections through a set of realizations conducted under a predefined experimental design<sup>7</sup>. One of the CMIP groups is ScenarioMIP, where models run the standard IPCC climate change scenarios<sup>8</sup>. Of particular interest for the purposes of this paper are two contrasting scenarios. The Shared Socioeconomic Pathway SSP2 coupled with the Representative Concentration Pathway RCP4.5 (SSP2-4.5), which consists in a middle-of-the-road socioeconomic scenario where future development follows historical trends and radiative forcing reaches 4.5 W/m<sup>2</sup> by 2100. This scenario leads to around 2.5–3.5 °C of increase in global mean surface temperature by the end of this century, compared to the preindustrial value<sup>9,10</sup>. In contrast, the SSP5-8.5 represents a fossil-fueled bonanza leading to 4.5–5.5 °C increase<sup>9,11</sup>; there is an ongoing debate whether this should be considered a “Business as usual” scenario or a catastrophic one<sup>12–14</sup>.

GeoMIP is another CMIP group that aims to study the effects of geoengineering<sup>15</sup>. Among GeoMIP experiments, G6sulfur aims to explicitly model SAI, and it consists of the SSP5-8.5 emissions trajectory plus the injection of the necessary aerosols to keep global and latitude-specific mean surface temperature increase in the SSP2-4.5 range<sup>16</sup>. Figure 1a presents the SSP5-8.5 global average near-surface temperature change from 2020 to 2100 for the 6 GCMs that participated in the G6sulfur experiment, while Fig. 1b presents the anomaly in

<sup>1</sup>Instituto de Ciencias de la Atmósfera, Universidad Nacional Autónoma de México, Av. Universidad 3004, Copilco Universidad, Coyoacán, 04510, Ciudad de México, CDMX, Mexico. <sup>2</sup>Programa de Investigación en Cambio Climático, Universidad Nacional Autónoma de México, Av. Universidad 3004, Copilco Universidad, Coyoacán, 04510, Ciudad de México, CDMX, Mexico. ✉e-mail: [rodrigo.munoz@atmosfera.unam.mx](mailto:rodrigo.munoz@atmosfera.unam.mx)

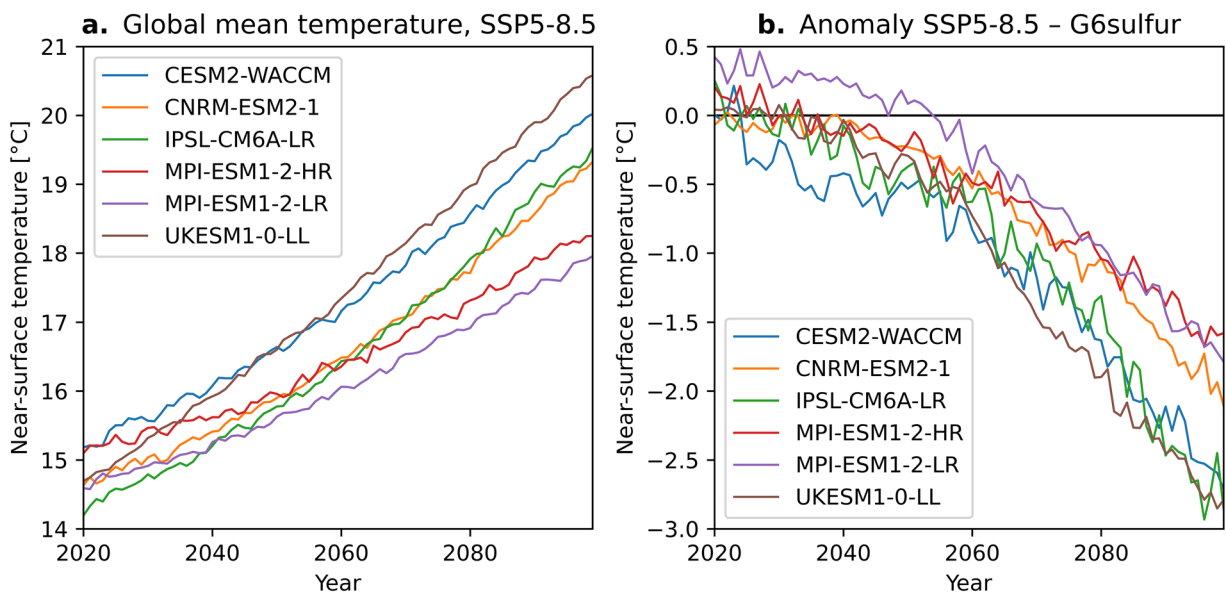


**Fig. 1** Scaling factors for GeoMIP-pattern. **(a)** Global mean near-surface temperature for the 6 GCMs that participated in the G6sulfur experiment, **(b)** Difference between G6sulfur and SSP5-8.5 global mean near-surface temperature.

global average near-surface temperature between the G6sulfur experiment and the SSP5-8.5 scenario for each model. Due to the GCM's different parametrizations for chemistry and stratospheric circulation, large regional variations arise, giving light to the uncertainty in geoengineering approaches<sup>16</sup>. In addition, while general temperature patterns align with the SSP2-4.5, other climate variables, such as precipitation, are overcompensated, showing large reductions and a heterogenous spatial pattern<sup>16</sup>.

SAI, SRM, and geoengineering in general are surrounded by ethical concerns<sup>17–20</sup>, particularly by the unilateral capability of state and non-state actors to start and stop a geoengineering program<sup>21–23</sup>. The termination shock, that is, a sudden conclusion of geoengineering and a fast onset of the avoided climate change, is expected to have disastrous consequences and is considered of particular concern<sup>24–28</sup>. Additionally, while simulations show geoengineering is successful in dampening global average temperature increase, regional and local impacts on climate are far less understood and their associated second-order effects on the Earth system and the global economy might offset the benefits derived from global climate change mitigation<sup>29–31</sup>. It is therefore imperative to conduct impact analyses on natural, economic and social systems on a regional scale to further understand the consequences of geoengineering.

An important limitation for conducting such studies is the sheer volume of data generated by GCMs and the large processing capabilities needed to run additional scenarios. Pattern scaling is a tool that can simplify the generation of climate projections<sup>32</sup>, allowing the focus to shift toward other aspects of the research<sup>33</sup>, and to strengthen uncertainty analysis with the generation of large ensembles and Monte Carlo simulations for probabilistic analysis. Pattern scaling consists, in the most general sense, in the determination of the marginal change of a local climate variable with respect to a unitary change of the global mean temperature<sup>34</sup>. While more complex regressions have been devised<sup>35–39</sup>, the most common and straightforward way to do this is by estimating an ordinary least squares linear regression for each cell in a GCM. In such a regression, the global mean temperature is the independent variable, also known as the scaling factor (Fig. 1a), and the dependent variable corresponds to the local climate variable<sup>40</sup>. Pattern scaling is generally done for annual values, but it is increasingly used for monthly values in order to calculate seasonal impacts<sup>40</sup>, which might be obscured in annual means. Given the level of variability at daily and hourly data, pattern scaling is not commonly considered for these kind of impact studies, as other methods are more appropriate, but its usefulness lies in the determination of strong climate change signals within larger time frame impact studies such as drought studies, ecological niche and potential distribution, basin balances, and economic analyses, and for custom scenario generation and probabilistic studies.

The scaling patterns can be used to reconstruct GCM output using a minimal amount of data and operations, and while the results are inherently imprecise, they have been shown to yield acceptable approximations<sup>41–43</sup>. Another use for pattern scaling is to generate a new climate scenario with the help of a climate emulator<sup>33</sup>. Climate emulators are simple models that calculate global mean temperature for any given emissions pathway. This output is then fed to the patterns as the scaling factor to generate the spatially explicit evolution of different climate variables without the need to run time- and resource-expensive GCMs. When using pattern scaling in this way, the main interest is then for the patterns to adequately capture the local trend in the given variable due to climate change. A useful way to evaluate whether a linear regression correctly captures the trend present in the data, or whether there could be a nonlinear behavior, is to test whether the residuals have remaining non-stationarities such as residual trends or if the errors of the regression behave approximately as a stationary

process. Here we formally investigate this assumption through the use of unit root tests<sup>44</sup>. To our knowledge, no research has applied such tests to validate whether pattern scaling adequately captures local trends—a gap this study aims to address.

In this paper, we present GeoMIP-pattern, a dataset based on GeoMIP G6sulfur output and the first pattern scaling dataset for the use in geoengineering studies. These patterns can be used to reproduce the G6sulfur output for 3 variables: mean near-surface temperature, relative humidity, and precipitation; they can also be used to generate custom geoengineering scenarios. Local variable values are reconstructed using two scaling factors: no-SAI global mean temperature (Fig. 1a) to obtain a no-SAI local value, and the global temperature difference between SAI and no-SAI scenarios (Fig. 1b), to adjust the local value to a SAI scenario; this allows for comparison studies between no-SAI and SAI scenarios. The dataset also includes validation measures for each pattern; of special interest are the use of unit root tests to evaluate stationarity in the regressions' residuals for a novel and robust validation of the presented data.

## Methods

Scaling patterns are generally derived from simple univariate linear regression using global temperature as the independent variable, known as the scaling factor, and the local value of temperature as the dependent variable<sup>39</sup>:

$$T_{l,y} = \alpha_l + \beta_l T_{g,y} \quad (1)$$

Where  $T_{l,y}$  is the model mean surface temperature for year  $y$  and a geographical location  $l$  defined by a pair of coordinates,  $\alpha_l, \beta_l$  are the regression intercept and slope parameters for location  $l$ , and  $T_{g,y}$  is the model average global mean surface temperature for year  $y$ . Every single variable for a given model consists of its ensemble mean as is commonly done for pattern scaling; since the GeoMIP runs contain one to three realizations, using each individual member is not useful to analyze intra-model variability. Input ScenarioMIP and GeoMIP data can be downloaded from the ESGF website (<https://aims2.llnl.gov/>).

Scaling patterns can be used for other variables such as precipitation  $P^{32,39,41,43}$ . However, it must be considered that precipitation is constrained as a positive variable and that model outputs exhibit large biases, rendering absolute changes expressed in  $mm$  less useful. A convenient way to circumvent this problem is by using a percentage change<sup>33</sup>, where changing temperature for precipitation percentage change in Eq. (1) results in:

$$\begin{aligned} 100 \cdot \frac{P_{l,y} - P_{l,h}}{P_{l,h}} &= \%P_{l,y} \\ \%P_{l,y} &= \alpha_l + \beta_l T_{g,y} \end{aligned} \quad (2)$$

Where  $P_{l,h}$  is the historical average value at location  $l$ . Equation (2) can also be applied to relative humidity, changing the variable  $P$  for the variable  $RH^{39}$ . For GeoMIP-pattern,  $P_{l,h}$  and  $RH_{l,h}$  have been calculated as the climatology from 1995–2014, as per recommendations from the IPCC<sup>45</sup>, and are also available in the dataset presented in this Data Descriptor.

Monthly scaling patterns also use the annual global temperature as the scaling factor, as is commonly done to have the strongest climate change signal and to allow coupling with climate emulators<sup>33,36,40,46,47</sup>, but coefficients are estimated for each monthly average temperature. Moreover, scaling patterns are commonly used in conjunction with reduced complexity climate models that simulate global mean annual temperature changes. The dependent variable is  $T_{l,y,m}$ , the model mean surface temperature for year  $y$ , month  $m$ , and location  $l^{39}$ :

$$T_{l,y,m} = \alpha_{l,m} + \beta_{l,m} T_{g,y} \quad (3)$$

Monthly patterns for precipitation and relative humidity are similarly derived from modifications to Eq. 2.

For this paper, we proposed the reconstruction of the G6sulfur variables using two patterns: the SSP5-8.5 pattern and a pattern associated with the difference between the G6sulfur and the SSP5-8.5 experiments. This is in line with the G6sulfur experiment approach, where the emissions trajectory remains the same as in SSP5-8.5, and the stratospheric sulfur injections are modulated to keep the global temperature in the range of the SSP2-4.5 scenario. Therefore, the equations for the temperature pattern are now:

$$T_{l,y,ssp585} = \alpha_{l,noSAI} + \beta_{l,noSAI} T_{g,y,ssp585} \quad (4)$$

$$\Delta T_{l,y,diff} = \alpha_{p,diff} + (-\beta_{l,diff}) \Delta T_{g,y,diff} \quad (5)$$

Where the  $ssp585$  subscript represents the model value in the SSP5-8.5 experiment model run, where no stratospheric aerosol injection takes place ( $noSAI$ ). The  $diff$  subscript represents difference between the G6sulfur and the SSP5-8.5 experiment, where stratospheric aerosol injection takes place (SAI); therefore,  $\Delta T_{g,y,diff}$  is the difference between the G6sulfur and the SSP5-8.5 global mean surface temperature for year  $y$ , while  $\Delta T_{l,y,diff}$  is the local difference between the G6sulfur and the SSP5-8.5 temperature for year  $y$  at location  $l$ . Temperature differences have been calculated between corresponding ensemble members.

The global mean surface temperature for the SSP5-8.5 experiment,  $T_{g,y,ssp585}$ , is the first scaling factor (Fig. 1a), and the second scaling factor is the difference between the global mean temperature in the SSP5-8.5 and the G6sulfur experiments (Fig. 1b), that is, the SAI temperature difference,  $T_{g,y,diff}$ . For details on how to use the derived coefficients to reconstruct a given SAI scenario, see the Usage Notes section.

The equations for precipitation (and for relative humidity, making the corresponding changes), where the global temperature remains as the scaling factor, are:

$$\%P_{l,y,ssp585} = \alpha_{l,noSAI} + \beta_{l,noSAI} T_{g,y,ssp585} \quad (6)$$

$$\%P_{l,y,diff} = \alpha_{l,diff} + (-\beta_{l,diff}) \Delta T_{g,y,diff} \quad (7)$$

The negative sign in Eq. (7) is also present to maintain consistency in the direction of change, given the signs present in the slope and the temperature change.

Figure 2 represents the patterns for each of the three variables. These values correspond to the map of the regression's slope coefficient of Eqs. (5, 7). Summary statistics can be found in Table 2 in the Validation Section and their spatial distribution is included in the dataset. To facilitate the interpretation, the *noSAI* minus *SAI* slope  $\beta_{l,diff}$  is multiplied by  $-1$ , allowing the reader to interpret the local temperature anomaly  $\Delta T_{l,y,diff}$  in the same way as the global temperature difference  $\Delta T_{g,y,diff}$ . Therefore, for each  $^{\circ}\text{C}$  reduction from the original SSP5-8.5 trajectory, the pattern indicates how local temperatures are expected to respond. For instance, a  $1^{\circ}\text{C}$  decrease in global temperature due to sulfur injection suggests that some regions in the Arctic could experience a temperature decrease of up to  $3^{\circ}\text{C}$  (Fig. 2a).

The dataset presented in this paper consists of a set of files of global maps of intercept and slope values using Eqs. (4, 5) for temperature, while using Eqs. (6, 7) for precipitation and relative humidity, selecting the corresponding dependent variable. The slopes are obtained for annual and monthly patterns and are presented in native model resolution. The linear regression has been done in Python using the *scikit-learn* package<sup>48</sup>. Figure 2 shows the multimodel mean *noSAI* minus *SAI* slope for each of the three variables, with dotted regions indicating where 33% of models disagree in the slope sign. This highlights the high level of disagreement among the original climate model outputs for precipitation and relative humidity—particularly at the monthly scale—and our framework appropriately retains this inter-model uncertainty in the emulated slopes.

Another set of files in the dataset consist in statistical values for the evaluation and validation of the patterns. For each pattern, we have calculated the standard deviation of the residuals (variable *RESIDS\_STD* in the NetCDF files), the root mean squared error (*RMSE*), the mean absolute error (*MAE*), the coefficient of determination  $R^2$  (*R2*), the regions where  $R^2 \geq 0.5$  (*R2\_MORE\_0.5*), the regions where  $R^2 \geq 0.9$  (*R2\_MORE\_0.9*), the p-value of the Augmented Dickey-Fuller Test ADF (*ADF\_RESIDS\_P*)<sup>49,50</sup>, the regions where  $ADF \leq 0.05$  (*ADF\_LESS\_0.05*), the p-value of the Kwiatkowski–Phillips–Schmidt–Shin Test KPSS, cropped between 0.01 and 0.1 as it is defined<sup>51</sup> (*KPSS\_RESIDS\_P*), the regions where  $KPSS \geq 0.05$  (*R2\_MORE\_0.9*), and the regions with a confirmatory unit root analysis where  $ADF < 0.05$  &  $KPSS > 0.05$  (*CONFIRM\_ANALYSIS\_NO\_TREND\_RESIDS\_0.05*)<sup>52</sup>. Both the KPSS and ADF tests have been calculated using the *statsmodels* python package<sup>53</sup>.

## Data Records

The dataset is available at figshare<sup>54</sup>; it contains the code used to generate the files, summary statistics for validation, and gridded datasets for each of the six models used in GeoMIP, which are briefly described in Table 1 from model metadata.

The root folder is “GeoMIP-pattern” and it contains a single file and five folders. The CSV file is named “score\_table.csv” and has a summary of the global average values of the slope and the statistical validation values for each annual and monthly pattern. The “script” folder contains the python scripts used to generate this dataset.

The “tas\_gav” folder contains NetCDF files with the annual global temperature (the scaling factor) for each climate model, and for the SSP5-8.5 experiment, the G6sulfur experiment, and the difference in temperature between the SSP5-8.5 and G6sulfur. For example, the files corresponding to the CESM2-WACCM model have the following names:

```
CESM2-WACCM_ssp585_ensemble_avg_tas_gav.nc
CESM2-WACCM_G6sulfur_ensemble_avg_tas_gav.nc
CESM2-WACCM_G6sulfur_ensemble_avg_tas_anom_gav.nc
```

The three remaining folders correspond to each of the variables analyzed in the dataset. “tas” corresponds to the surface air temperature, “pr” to the precipitation, and “hurs” to the relative humidity. The folder for each variable has a similar structure, separating monthly and annual data and having specific subfolders for historical climatologies, pattern slopes and intercept coefficients, and validation variables. For example, the precipitation folder structure is the following:

```
pr/
  annual/
    historical/
    patterns/
    score/
  monthly/
    historical/
    patterns/
    score/
```

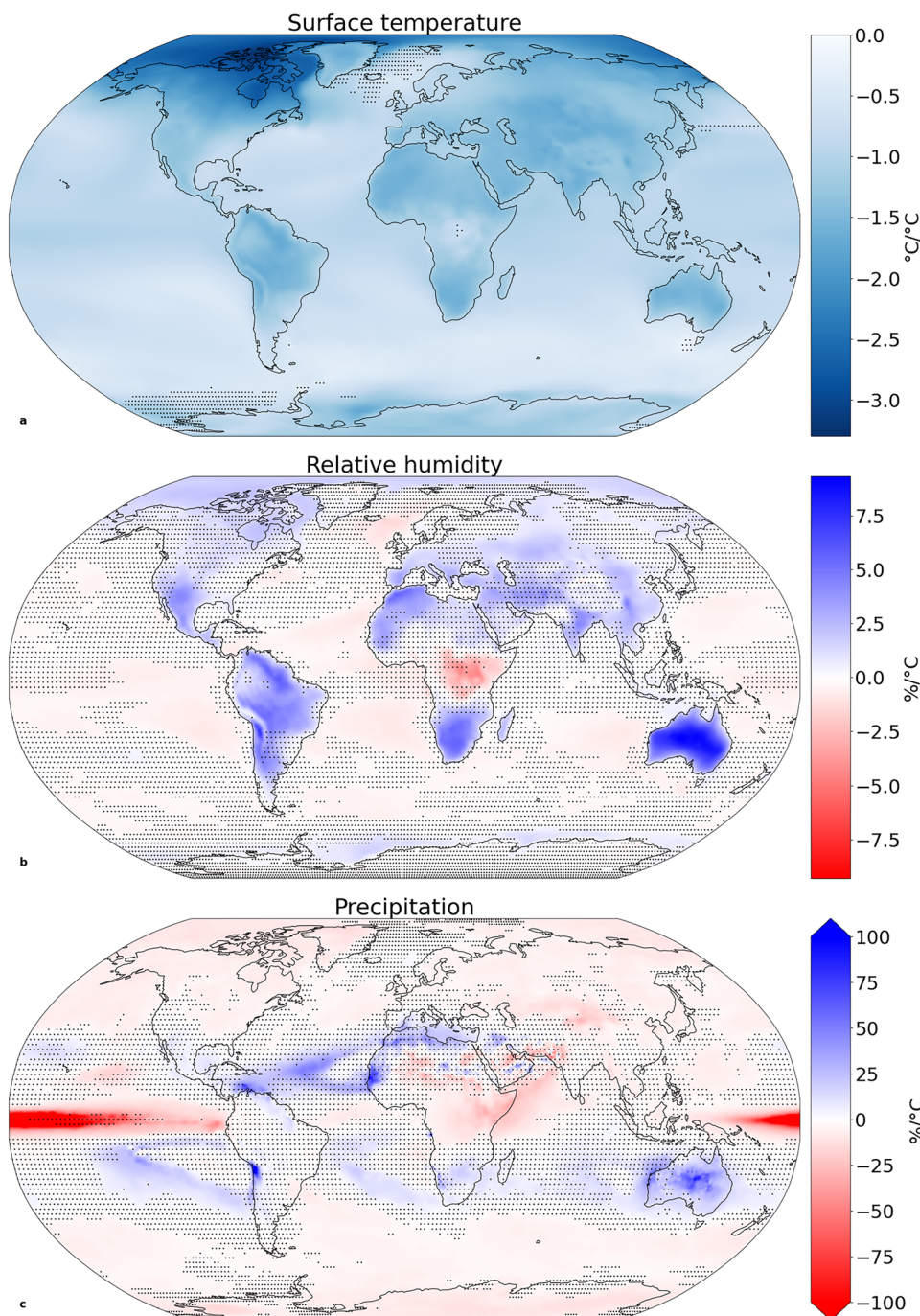


**Fig. 2** Multimodel mean *noSAI* minus *SAI* regression slope coefficient derived using a linear regression between the global temperature and local variable differences between the SSP5-8.5 and G6sulfur experiments, as represented in Eqs. (5, 7); dotted regions represent where 33% of the GCM model patterns disagree in the slope sign. (a) near-surface temperature, (b) relative humidity, and (c) precipitation.

The “*patterns*” subfolder has the SSP5-8.5 and the anomaly patterns. The files are named as follows, where VARIABLE can be either *tas*, *pr*, or *hurs*, and MODEL is one of the six models in Table 1:

MODEL\_ssp585\_tas\_annual\_pattern.nc  
MODEL\_G6sulfur\_tas\_annual\_pattern\_anom.nc

The *score* folder contains the statistical values for the validation of the patterns, named as follows:

MODEL\_G6sulfur\_tas\_annual\_pattern\_anom\_score.nc  
MODEL\_ssp585\_tas\_annual\_pattern\_score.nc

Model	Institution	Country	Atmospheric grid resolution
CESM2-WACCM	NCAR	USA	192 × 288 cells
CNRM-ESM2-1	CNRM-CERFACS	France	128 × 256 cells
IPSL-CM6A-LR	IPSL	France	143 × 144 cells
MPI-ESM1-2-HR	MPI-M, DKRZ, DWD	Germany	192 × 384 cells
MPI-ESM1-2-LR	MPI-M, DKRZ, DWD, AWI	Germany	96 × 192 cells
UKESM1-0-LL	NIWA, MOHC, NIMS-KMA	UK	144 × 192 cells

**Table 1.** GeoMIP models summary.

Variable	Period	Slope	Slope std	RMSE	RMSE std	KPSS & ADF	KPSS & ADF std
tas	Annual	1.010	0.0237	0.4661	0.1212	0.9995	0.0006
	Monthly	1.010	0.0515	0.915	0.2513	0.9987	0.0018
pr	Annual	-4.763	9.336	66.99	59.85	0.9990	0.0003
	Monthly	72.70	62.26	2404	2579	0.9965	0.0020
hurs	Annual	0.326	0.1299	1.890	0.3047	0.9981	0.0004
	Monthly	0.385	0.1872	4.816	0.8584	0.9985	0.0013

**Table 2.** Summary statistics for the GeoMIP-pattern dataset. The variable names correspond as follows: tas – surface temperature, pr – precipitation, hurs – relative humidity.

The *pr* and *hurs* folders have a similar structure to the *tas* one; however, the files contain an additional indicator in their name: *perc*, to indicate that patterns have been calculated using percentage changes. Additionally, these two variables have a “historical” subfolder, containing the historical climatological values, for use in calculating the percentage changes and reconstructing the GeoMIP output model data (see usage notes).

MODEL\_historical\_ensemble\_avg\_climatology\_VARIABLE.nc

Monthly data has a similar naming convention; however, each file has a month indicator ranging from “01” to “12”.

## Technical Validation

The confirmatory unit root analysis<sup>52</sup> is the main tool used in this paper for the evaluation of the validity of the patterns, and a novel method for pattern scaling validation which has not been used before in this field. Both the Augmented Dickey-Fuller (ADF)<sup>49,50</sup> and the KPSS test<sup>51</sup> are unit root tests, that is, they are used to evaluate whether the regressions’ residuals exhibit non-stationarities such as remaining trends. We extend the approach used by Estrada *et al.*<sup>55</sup> in which the ADF test is used to evaluate the adequacy of an emulator of a biophysical crop model. If deviations from the spatial pattern derived from Eqs. (1–7) are transitory, then the trend in global temperatures adequately captures the trend in the local variable of interest. In such a case, the residuals of such regression will be stationary processes. On the contrary, if deviations from the estimated spatial patterns are persistent or permanent, the residuals of the regressions would be non-stationary. Unit root tests are commonly used to discriminate between nonstationary and stationary time series, being the ADF test the most widely used in the literature. The ADF test, for the specification of interest, where a constant and trend have not been considered as exogenous variables, involves estimating the following regression:

$$\Delta y_t = \gamma y_{t-1} + \sum_{k=1}^K \delta_k y_{t-k} + \varepsilon_t \quad (8)$$

Where  $\sum_{k=1}^K \delta_k y_{t-k}$  are additional terms to correct for autocorrelation. If  $\gamma = 0$  the null hypothesis is accepted and the time series  $y_t$  is considered to contain a unit root. Under the alternative hypothesis,  $y_t$  is stationary around zero. In addition, the power of the ADF test goes to zero (i.e., the null is never rejected) when a deterministic trend is present in  $y_t$  but omitted in regression (8), and the test will also be biased towards non-rejection if there are structural changes in the trend parameters of  $y_t$ <sup>56</sup>. For the application at hand, the ADF will likely not reject the null hypothesis if there are persistent deviations from the estimated scaling patterns, independently if the non-stationarities are due to the presence of a unit root in the regression’s residuals, omitted trends or structural changes<sup>55</sup>.

Contrary to the ADF test, the KPSS test’s null hypothesis is that the time series is stationary. The KPSS procedure consists in estimating the following regression<sup>51</sup>:

$$y_t = c + z_t + e_t \quad (9)$$

$$z_t = z_{t-1} + \nu_t \quad (10)$$

Where  $c$  is the intercept, and  $e_t$  and  $\nu_t$  are independent and identically distributed stationary processes. If the variance of  $\nu_t$  is zero, the test suggests that  $y_t$  is stationary around a constant. The omission of a deterministic

trend or the presence of structural changes in the trend parameters, would severely bias the test towards the rejection of the null of stationarity<sup>44</sup>. The ADF and KPSS tests are commonly used together for gaining confidence if both tests lead to the same conclusion. This is sometimes referred to as a confirmatory analysis<sup>44,52,57</sup>.

With a chosen significance threshold of 0.05, ADF's null hypothesis is rejected if the test is significant ( $p < 0.05$ ), suggesting that there are no remaining relevant nonstationarities in the residuals, and if the KPSS test is not significant ( $p > 0.05$ ) the null hypothesis is not rejected, indicating that one cannot reject the absence of nonstationarities in the residuals. By testing for both the ADF and the KPSS, we can strengthen the conclusion that there are no remaining nonstationarities in the residuals<sup>52</sup>. Both tests have been implemented using the Python package *statsmodels*<sup>53</sup>, using the Bayesian Information Criterion (BIC) to determine the lag length in the ADF test, and the Newey-West estimator and bandwidth for the KPSS test. The dataset includes the p-value for each position  $p$ , where the KPSS p-value is cropped between 0.01 and 0.1 for which the test statistic is defined<sup>52</sup>. Additionally, the dataset includes the regions where the tests are or aren't significant at the 0.05 threshold, and the regions where ADF is significant and KPSS is not.

Table 2 contains data for the anomaly slope for surface temperature (tas), precipitation (pr), and relative humidity (hurs), showing the multimodel mean percentage of sites where both tests lead to the same conclusion (KPSS & ADF column), and indicating that in that percentage of the planet, the residuals show no significant deviations from stationarity and therefore, the estimated scaling pattern is adequate. The results show that, for every variable and for both annual and monthly patterns, in more than 99.5% of the planet the pattern slope correctly captures the underlying trend in the GeoMIP data output. This consistency is more striking in the wake of expectations when using a p-value threshold of 0.05, where one anticipates a 5% margin for error. Additionally, given the large number of slope values per model — such as the CESM2-WACCM's atmospheric grid with  $0.9375^\circ \times 1.25^\circ$  resolution and a total of 55,296 cell values — the high percentage of correctly captured trends reinforces confidence in the robustness of the linear pattern. The KPSS & ADF std column indicates the standard deviation of the percentage of the globe that passes the confirmatory analysis. Considering the large spatial sample size and the p-value threshold, and the fact that all models within one standard deviation correctly capture the trend in more than 99.5% of the planet, it is evident that the pattern scaling can replicate modeled trends in variables due to anthropogenic intromission in the climate system.

Table 2 and the underlying dataset additionally include other statistical values for the validation of the pattern scaling. These are not analyzed in depth in this paper but are provided for users of the dataset to conduct other validation analyses if needed. The validation scores have also been calculated for the *noSAI* patterns and the values are available in the corresponding dataset files; as pattern scaling is well established for standard CMIP experiments, there has been extensive validation elsewhere<sup>41–43</sup>.

We have additionally analyzed the spatial distribution of the confirmatory analysis, as shown in Fig. 3. This figure indicates regions where there is still nonstationarities in the residuals, as given by points where the confirmatory analysis is rejected for at least one model. For the three studied variables, there are no regions where more than a third of the models indicate that there are still nonstationarities in the residuals, and it can be seen that the vast majority of the globe consists of regions where all models indicate that the trend is captured correctly. The places where nonstationarities are still present in the residuals are scattered around the globe, and most of them indicate that the residuals of only one model pattern still have nonstationarities.

## Usage Notes

The first possible usage for the GeoMIP-pattern dataset is a low-data requirement reconstruction of the SSP5-8.5 and G6sulfur GCM annual and monthly output data for temperature, precipitation, and relative humidity. For the SSP5-8.5 model output, Eq. (4) may be used for local temperature values, while for precipitation, Eq. (11) follows from Eqs. (2, 6):

$$P_{l,y,ssp585} = P_{l,h} \frac{(100 + \alpha_{l,noSAI} + \beta_{l,noSAI} T_{g,y,ssp585})}{100} \quad (11)$$

For the G6sulfur output, Eqs. (4, 5) result in Eq. (12) and Eqs. (2, 7) yield Eq. (13):

$$T_{l,y,G6sulfur} = \alpha_{l,noSAI} + \beta_{l,noSAI} T_{g,y,ssp585} + \alpha_{l,diff} - \beta_{l,diff} \Delta T_{g,y,diff} \quad (12)$$

$$P_{l,y,G6sulfur} = P_{l,h} (100 + \alpha_{l,noSAI} + \beta_{l,noSAI} T_{g,y,noSAI}) (100 + \alpha_{l,diff} - \beta_{l,diff} \Delta T_{g,y,diff}) \quad (13)$$

The second possible use of the dataset consists in the generation of a custom SAI scenario, whereby a climate emulator is fed with an emissions and aerosol trajectory to generate  $\Delta T_{g,y,noSAI}$  and  $\Delta T_{g,y,anom}$ . In this case the relevant dataset value is the slope. Based on the previous equations, the resulting local SAI variable values anomaly,  $\Delta T_{l,y,SAP}$ , are:

$$\Delta T_{l,y,SAI} = \beta_{l,noSAI} \Delta T_{g,y,noSAI} - \beta_{l,diff} \Delta T_{g,y,diff} \quad (14)$$

$$\Delta \% P_{l,y,SAI} = \frac{(100 + \beta_{l,noSAI} \Delta T_{g,y,noSAI}) (100 - \beta_{l,diff} \Delta T_{g,y,diff})}{100} - 100 \quad (15)$$

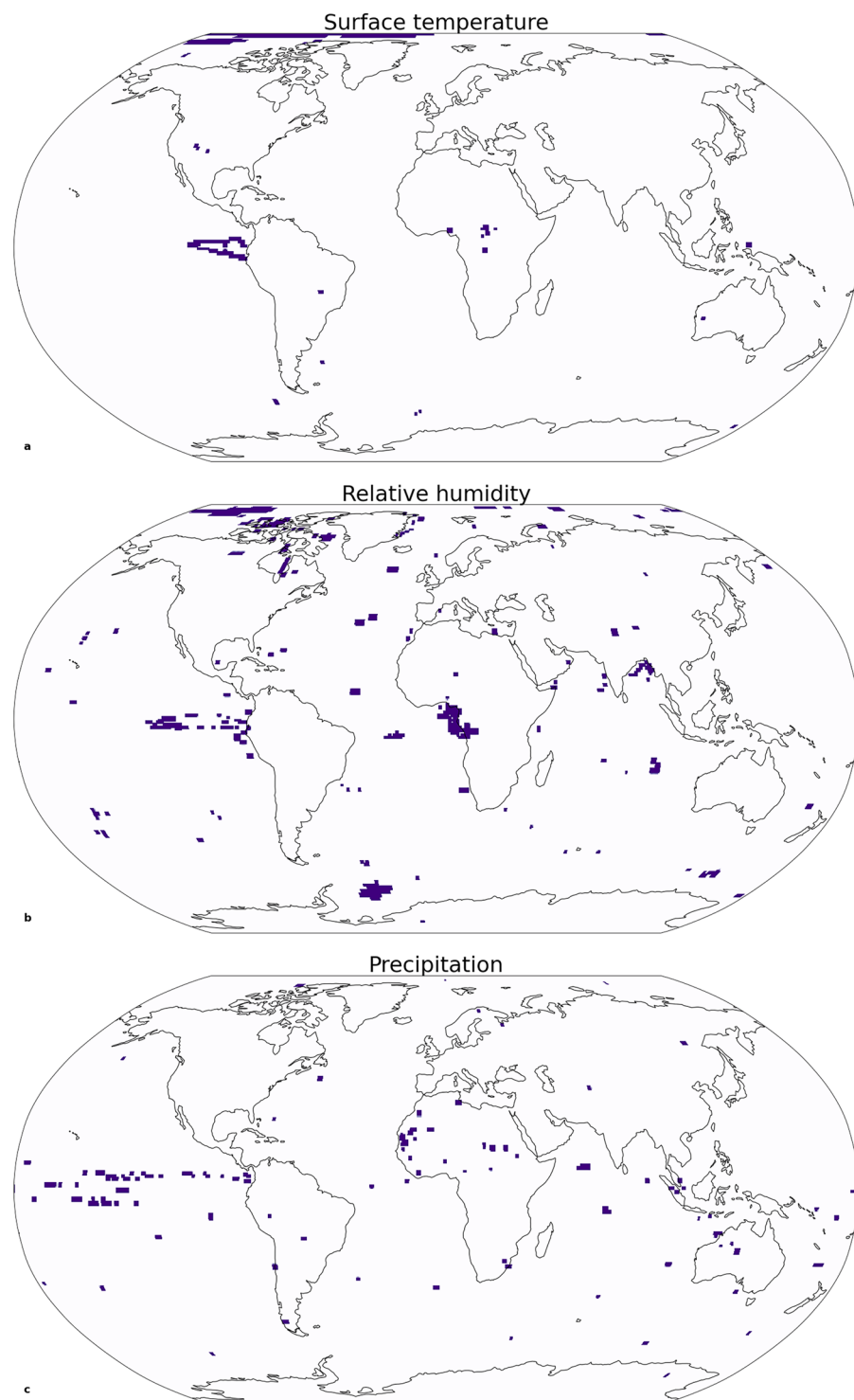


**Fig. 3** Regions where a given percentage of model patterns indicate that there is still a trend in the residuals in at least one model, as indicated by the confirmatory analysis. (a) temperature, (b) relative humidity, (c) precipitation.

Finally, the local temperature value for a given year,  $T_{l,y,SAI}$  will be obtained by applying the obtained anomaly to historical values,  $T_{l,h,obs}$ , using the delta method for constructing fields of change<sup>33,58</sup>:

$$T_{l,y,SAI} = \Delta T_{l,y,SAI} + T_{l,h,obs} \quad (16)$$

Precipitation is derived in an analogous fashion:

$$P_{l,y,SAI} = P_{l,h,obs} (1 + \Delta \% P_{l,y,SAI}) \quad (17)$$

Care must be taken not to forget that emulated data produced by this dataset originates from a linear regression and that pattern scaling is based on a statistical method. As such, hydrodynamic effects such as nonlinear dynamic feedbacks or teleconnections might be lost. However, the statistical validation using unit root tests show that this simplification does correctly capture the broad trends, even if they are the result of a complex, chaotic, and non-linear climate system.

## Code availability

The python script used to obtain the dataset is part of the dataset release itself and can be publicly consulted.

Received: 9 January 2025; Accepted: 1 July 2025;

Published online: 01 August 2025

## References

1. Caldeira, K., Bala, G. & Cao, L. The Science of Geoengineering. *Annu. Rev. Earth Planet. Sci.* **41**, 231–256 (2013).
2. Ming, T., de Richter, R., Liu, W. & Caillol, S. Fighting global warming by climate engineering: Is the Earth radiation management and the solar radiation management any option for fighting climate change? *Renewable and Sustainable Energy Reviews* **31**, 792–834 (2014).
3. Hulme, M. Climate change: Climate engineering through stratospheric aerosol injection. *Progress in Physical Geography: Earth and Environment* **36**, 694–705 (2012).
4. Toohey, M., Jia, Y., Khanal, S. & Tegtmeier, S. Stratospheric residence time and the lifetime of volcanic stratospheric aerosols. *Atmos. Chem. Phys.* **25**, 3821–3839 (2025).
5. Lee, W. R. *et al.* Quantifying the Efficiency of Stratospheric Aerosol Geoengineering at Different Altitudes. *Geophysical Research Letters* **50**, e2023GL104417 (2023).
6. Visioni, D. *et al.* Opinion: The scientific and community-building roles of the Geoengineering Model Intercomparison Project (GeoMIP) – past, present, and future. *Atmos. Chem. Phys.* **23**, 5149–5176 (2023).
7. Eyring, V. *et al.* Overview of the Coupled Model Intercomparison Project Phase 6 (CMIP6) experimental design and organization. *Geosci. Model Dev.* **9**, 1937–1958 (2016).
8. O'Neill, B. C. *et al.* The Scenario Model Intercomparison Project (ScenarioMIP) for CMIP6. *Geosci. Model Dev.* **9**, 3461–3482 (2016).
9. Riahi, K. *et al.* The Shared Socioeconomic Pathways and their energy, land use, and greenhouse gas emissions implications: An overview. *Global Environmental Change* **42**, 153–168 (2017).
10. Fricko, O. *et al.* The marker quantification of the Shared Socioeconomic Pathway 2: A middle-of-the-road scenario for the 21st century. *Global Environmental Change* **42**, 251–267 (2017).
11. Riahi, K. *et al.* RCP 8.5—A scenario of comparatively high greenhouse gas emissions. *Climatic Change* **109**, 33–57 (2011).
12. Hausfather, Z. & Peters, G. P. Emissions – the ‘business as usual’ story is misleading. *Nature* **577**, 618–620 (2020).
13. Ho, E., Budescu, D. V., Bosetti, V., Van Vuuren, D. P. & Keller, K. Not all carbon dioxide emission scenarios are equally likely: a subjective expert assessment. *Climatic Change* **155**, 545–561 (2019).
14. Connolly, R., Connolly, M., Carter, R. M. & Soon, W. How Much Human-Caused Global Warming Should We Expect with Business-As-Usual (BAU) Climate Policies? A Semi-Empirical Assessment. *Energies* **13**, 1365 (2020).
15. Kravitz, B. *et al.* The Geoengineering Model Intercomparison Project (GeoMIP). *Atmospheric Science Letters* **12**, 162–167 (2011).
16. Kravitz, B. *et al.* The Geoengineering Model Intercomparison Project Phase 6 (GeoMIP6): simulation design and preliminary results. *Geosci. Model Dev.* **8**, 3379–3392 (2015).
17. Wieding, J., Stubenrauch, J. & Ekardt, F. Human Rights and Precautionary Principle: Limits to Geoengineering, SRM, and IPCC Scenarios. *Sustainability* **12**, 8858 (2020).
18. Pamplany, A., Gordijn, B. & Brereton, P. The Ethics of Geoengineering: A Literature Review. *Sci Eng Ethics* **26**, 3069–3119 (2020).
19. Biermann, F. *et al.* Solar geoengineering: The case for an international non-use agreement. *WIREs Climate Change* **13**, e754 (2022).
20. McDonald, M. Geoengineering, climate change and ecological security. *Environmental Politics* **32**, 565–585 (2023).
21. Stephens, J. C., Kashwan, P., McLaren, D. & Surprise, K. Toward Dangerous US Unilateralism on Solar Geoengineering. *Environmental Politics* **32**, 171–173 (2023).
22. Surprise, K. Geopolitical ecology of solar geoengineering: from a ‘logic of multilateralism’ to logics of militarization. *Journal of Political Ecology* **27** (2020).
23. Eliasou, A. Avoiding Moonraker: Averting Unilateral Geoengineering Efforts. *U. Pa. J. Int'l L.* **43**, 429 (2021).
24. Abatayo, A. L., Bosetti, V., Casari, M., Ghidoni, R. & Tavoni, M. Solar geoengineering may lead to excessive cooling and high strategic uncertainty. *Proc. Natl. Acad. Sci. U.S.A.* **117**, 13393–13398 (2020).
25. Finus, M. & Furini, F. On the credibility of threats to avoid the deployment of solar geoengineering. *Environ Econ Policy Stud* (2024)
26. Reynolds, J. L. Is solar geoengineering ungovernable? A critical assessment of governance challenges identified by the Intergovernmental Panel on Climate Change. *WIREs Climate Change* **12**, e690 (2021).
27. Lin, A. C. Avoiding lock-in of solar geoengineering. *N. Yk. L. Rev.* **47**, 139 (2020).
28. Malm, A. The Future is the Termination Shock: On the Antinomies and Psychopathologies of Geoengineering. Part Two. *Historical Materialism* **31**.1, 3–61 (2023).
29. Visioni, D. *et al.* Identifying the sources of uncertainty in climate model simulations of solar radiation modification with the G6sulfur and G6solar Geoengineering Model Intercomparison Project (GeoMIP) simulations. *Atmos. Chem. Phys.* **21**, 10039–10063 (2021).
30. Ricke, K., Wan, J. S., Saenger, M. & Lutsko, N. J. Hydrological Consequences of Solar Geoengineering. *Annual Review of Earth and Planetary Sciences* **51**, 447–470 (2023).
31. Kravitz, B. & MacMartin, D. G. Uncertainty and the basis for confidence in solar geoengineering research. *Nat Rev Earth Environ* **1**, 64–75 (2020).
32. Lynch, C., Hartin, C., Bond-Lamberty, B. & Kravitz, B. An open-access CMIP5 pattern library for temperature and precipitation: description and methodology. *Earth Syst. Sci. Data* **9**, 281–292 (2017).
33. Estrada, F., Calderón-Bustamante, O., Botzen, W., Velasco, J. A. & Tol, R. S. J. AIRCC-Clim: A user-friendly tool for generating regional probabilistic climate change scenarios and risk measures. *Environmental Modelling & Software* **157**, 105528 (2022).
34. Herger, N., Sanderson, B. M. & Knutti, R. Improved pattern scaling approaches for the use in climate impact studies. *Geophysical Research Letters* **42**, 3486–3494 (2015).
35. Castruccio, S. *et al.* Statistical Emulation of Climate Model Projections Based on Precomputed GCM Runs\*. *Journal of Climate* **27**, 1829–1844 (2014).
36. Tebaldi, C. & Arblaster, J. M. Pattern scaling: Its strengths and limitations, and an update on the latest model simulations. *Climatic Change* **122**, 459–471 (2014).
37. Kasim, M. F. *et al.* Building high accuracy emulators for scientific simulations with deep neural architecture search. *Mach. Learn.: Sci. Technol.* **3**, 015013 (2022).

38. Beusch, L., Gudmundsson, L. & Seneviratne, S. I. Emulating Earth system model temperatures with MESMER: from global mean temperature trajectories to grid-point-level realizations on land. *Earth Syst. Dynam.* **11**, 139–159 (2020).
39. Nath, S., Lejeune, Q., Beusch, L., Seneviratne, S. I. & Schleussner, C.-F. MESMER-M: an Earth system model emulator for spatially resolved monthly temperature. *Earth Syst. Dynam.* **13**, 851–877 (2022).
40. Kravitz, B. & Snyder, A. Pangeo-Enabled ESM Pattern Scaling (PEEPS): A customizable dataset of emulated Earth System Model output. *PLOS Clim* **2**, e0000159 (2023).
41. Tebaldi, C. & Knutti, R. Evaluating the accuracy of climate change pattern emulation for low warming targets. *Environ. Res. Lett.* **13**, 055006 (2018).
42. Kravitz, B., Lynch, C., Hartin, C. & Bond-Lamberty, B. Exploring precipitation pattern scaling methodologies and robustness among CMIP5 models. *Geosci. Model Dev.* **10**, 1889–1902 (2017).
43. Wells, C. D., Jackson, L. S., Maycock, A. C. & Forster, P. M. Understanding pattern scaling errors across a range of emissions pathways. *Earth Syst. Dynam.* **14**, 817–834 (2023).
44. Maddala, G. S. & Kim, I.-M. Unit Roots, Cointegration, and Structural Change. <https://doi.org/10.1017/CBO9780511751974> (Cambridge University Press, 1999).
45. IPCC. Climate Change 2021: The Physical Science Basis. Contribution of Working Group I to the Sixth Assessment Report of the Intergovernmental Panel on Climate Change. Cambridge University Press. (2021)
46. Osborn, T. J., Wallace, C. J., Harris, I. C. & Melvin, T. M. Pattern scaling using ClimGen: monthly-resolution future climate scenarios including changes in the variability of precipitation. *Climatic Change* **134**, 353–369 (2016).
47. Zelazowski, P., Huntingford, C., Mercado, L. M. & Schaller, N. Climate pattern-scaling set for an ensemble of 22 GCMs – adding uncertainty to the IMOGEN version 2.0 impact system. *Geosci. Model Dev.* **11**, 541–560 (2018).
48. Scikit-learn: Machine Learning in Python, Pedregosa *et al.* JMLR **12**, pp. 2825–2830, (2011).
49. Dickey, D. A. & Fuller, W. A. Distribution of the Estimators for Autoregressive Time Series with a Unit Root. *J Am Statist Assoc* **74**, 427–431 (1979).
50. Said, S. E. & Dickey, D. A. Testing for unit roots in autoregressive-moving average models of unknown order. *Biometrika* **71**, 599–607 (1984).
51. Kwiatkowski, D., Phillips, P. C. B., Schmidt, P. & Shin, Y. Testing the null hypothesis of stationarity against the alternative of a unit root. *Journal of Econometrics* **54**, 159–178 (1992).
52. Perron, P. & Ng, S. Useful Modifications to some Unit Root Tests with Dependent Errors and their Local Asymptotic Properties. *The Review of Economic Studies* **63**, 435 (1996).
53. Seabold, S. & J Perktold. statsmodels: Econometric and statistical modeling with python. *Proceedings of the 9th Python in Science Conference*. (2010).
54. Muñoz-Sánchez *et al.* GeoMIP-Pattern – a pattern scaling dataset for efficient generation of custom geoengineering scenarios <https://doi.org/10.6084/m9.figshare.2816559> (2025).
55. Estrada, F. *et al.* Model emulators for the assessment of regional impacts and risks of climate change: A case study of rainfed maize production in Mexico. *Front. Environ. Sci.* **11**, 1027545 (2023).
56. Perron, P. The Great Crash, the Oil Price Shock, and the Unit Root Hypothesis. *Econometrica* **57**, 1361 (1989).
57. Carrion-i-Silvestre, J. L., Sansó-i-Rosselló, A. & Ortuño, M. A. Unit root and stationarity tests' wedding. *Economics Letters* **70**, 1–8 (2001).
58. IPCC. IPCC Technical Guidelines for Assessing Climate Change Impacts and Adaptations. Part of the IPCC Special Report to the First Session of the Conference of the Parties to the UN Framework Convention on Climate Change, Working Group II, Intergovernmental Panel on Climate Change. University College London, United Kingdom and Center for Global Environmental Research, National Institute for Environmental Studies, Tsukuba, Japan (1994)

## Acknowledgements

The authors would like to thank the Degrees Initiative for the funding given to conduct this research. R.M. would also like to thank Conahcyt for the doctoral scholarship that allowed him to work on this paper.

## Author contributions

R.M. did the main processing for the database and wrote the initial draft, F.E. had the initial idea for the paper, all the authors participated in meetings to discuss the paper, participated in its writing and revision.

## Competing interests

The authors declare no competing interests.

## Additional information

**Correspondence** and requests for materials should be addressed to R.M.-S.

**Reprints and permissions information** is available at [www.nature.com/reprints](http://www.nature.com/reprints).

**Publisher's note** Springer Nature remains neutral with regard to jurisdictional claims in published maps and institutional affiliations.



**Open Access** This article is licensed under a Creative Commons Attribution-NonCommercial-NoDerivatives 4.0 International License, which permits any non-commercial use, sharing, distribution and reproduction in any medium or format, as long as you give appropriate credit to the original author(s) and the source, provide a link to the Creative Commons licence, and indicate if you modified the licensed material. You do not have permission under this licence to share adapted material derived from this article or parts of it. The images or other third party material in this article are included in the article's Creative Commons licence, unless indicated otherwise in a credit line to the material. If material is not included in the article's Creative Commons licence and your intended use is not permitted by statutory regulation or exceeds the permitted use, you will need to obtain permission directly from the copyright holder. To view a copy of this licence, visit <http://creativecommons.org/licenses/by-nc-nd/4.0/>.

© The Author(s) 2025